ACS Biomaterials SCIENCE & ENGINEERING

pubs.acs.org/journal/abseba

Article

# Development of a Uricase-Free Colorimetric Biosensor for Uric Acid Based on PPy-Coated Polyoxometalate-Encapsulated Fourfold Helical Metal–Organic Frameworks

Ying-Ying Wang, Hai-Feng Zhang, Dong-Hui Wang, Ning Sheng, Gong-Guo Zhang, Ling Yin, and Jing-Quan Sha*

Cite This: *ACS Biomater. Sci. Eng.* 2020, 6, 1438–1448

Read Online

ACCESS | Metrics & More | Article Recommendations | Supporting Information

**ABSTRACT:** Developing a new cost-effective and reliable approach used for the detection of uric acid (UA) with no requirement of uricase is still very challenging. Herein, an easily realized, cost-effective, and uricase-free approach is reported for selective colorimetric biosensing of UA utilizing polypyrrole (PPy)-coated polyoxometalate-encapsulated fourfold helical metal–organic frameworks $Ag_5[bimt]_2[PMo_{12}O_{40}]\cdot 2H_2O$ ($Ag_5PMo_{12}$) as a monolithic peroxidase mimic. It is demonstrated that the as-obtained $Ag_5PMo_{12}$@PPy possesses excellent peroxidase-like activity originated from the synergistic effect to induce catalytic oxidation of colorless 3,3′,5,5′-tetramethylbenzidine (TMB) to green oxTMB in the presence of $H_2O_2$. Then, the green oxTMB can be selectively converted to colorless TMB induced by UA; thus, UA can inhibit the catalytic oxidation of TMB. Based on these results, a uricase-free colorimetric biosensor for UA is achieved with a linear detection range of 1–50 $\mu$M and a detection limit of 0.47 $\mu$M. More importantly, the developed biosensor is suited for simple-operated and good reliable UA detection in clinical samples, showing promising application ability in clinical diagnosis and relative fields.

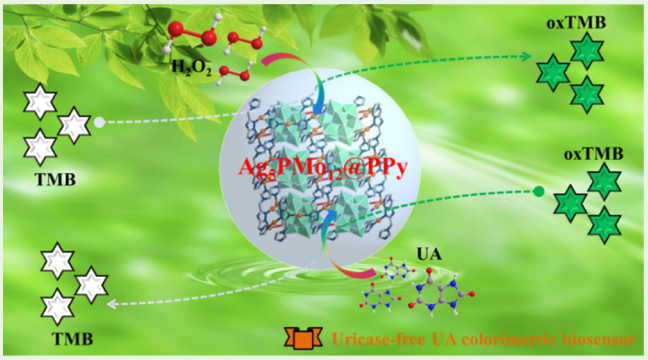


**KEYWORDS:** *uric acid, colorimetric detection, uricase-free, helical MOFs, PPy*

## INTRODUCTION

Uric acid (UA), as a nitrogen-containing final product from the metabolism process of purine, is an important biochemical component in human serum and urine fluids, which can be used as a disease diagnosis indicator.[1,2] The normal UA levels in serum and urine fluids are 0.24–0.52 and 1.4–4.4 mM, respectively.[3] As we know, the abnormal UA level may cause various pathological symptoms, such as gouty arthritis, urolithiasis, hyperuricaemia, Lesch-Nyhan syndrome, and and so forth.[4−6] Thus, precise and rapid UA level detection is of vital significance in disease diagnosis and related complication prevention.

In the past decades, a series of detection means toward the UA content have been reported, such as high-performance liquid chromatography,[7,8] capillary electrophoresis,[9] fluorescence (FL) spectroscopy,[10] electrochemical technique,[11] and so on. In spite of this, the abovementioned methods still encompass some limitations, such as high cost, time consumption, and intricate sample pretreatment. In contrast to these methods, colorimetric sensing is more attractive and promising with the advantages of being cheap, visualizable, and sensitive. At present, many colorimetric sensors for the UA detection are based on the mechanism of catalytic oxidation.[12,13] More specifically, the reaction is mostly achieved based on 3,3′,5,5′-tetramethylbenzidine (TMB) catalytic oxidation through hydroxyl radical (•OH) generated from the decomposition of $H_2O_2$ in the presence of peroxidase mimics. For example, the Zhang group reported a UA colorimetric sensor that relies on the peroxidase-like activity of g-$C_3N_4$ nanosheets with the help of uricase.[12] Zhao and co-authors proposed the Au nanocluster stabilized with bovine serum albumin for the colorimetric determination of the UA level.[14] However, for most of these UA colorimetric sensors, uricase with vulnerable activity is still essential, which may result in the poor stability and repeatability (see Table S1). Until now, only two UA colorimetric sensors without uricase have been explored.[45,46] Therefore, we are devoted to searching another alternative material for sensitive and rapid

Received: December 16, 2019
Accepted: January 31, 2020
Published: February 1, 2020






https://dx.doi.org/10.1021/acsbiomaterials.9b01922
*ACS Biomater. Sci. Eng.* 2020, 6, 1438–1448

**Scheme 1. Schematic Description of the Fabrication Process of $Ag_5PMo_{12}$@PPy and the Corresponding Colorimetric UA Biosensor by Utilizing $Ag_5PMo_{12}$@PPy as Peroxidase Mimics**

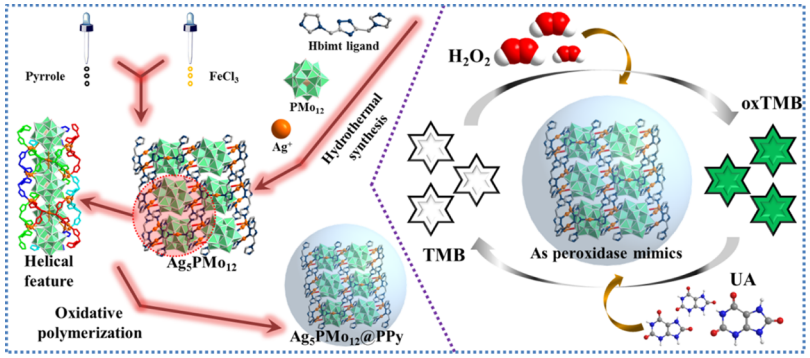


UA colorimetric detection in the absence of any natural enzyme to break the abovementioned bottleneck.[47]

As nanoscale versatile metal oxide clusters, polyoxometalates (POMs) have been explored deeply in catalysis technology, electrochemistry and material science because of their acid/base and redox properties with tunability.[14−17] Especially, Keggin-type $PW_{12}O_{40}$ and $SiW_{12}O_{40}$ and tetra-nuclear Zr-substituted $[P_2W_{16}O_{59}]^{12-}$ modified with O-donor peroxide ligands with excellent peroxidase-like activities have been studied for small molecule detection.[18−20] However, the poor recovery issues resulting from good water solubility shadowed their highlights and hindered their application outside the laboratory. Based on some stable metal−organic frameworks (MOFs) with peroxidase-like activity being explored as colorimetric biosensors (e.g., MOF-808),[21−24] consequently, POMs have been incorporated with MOFs to fabricate POMOFs with excellent stability and superior activity.[25] Among these POMOFs reported in the literature, $Cu_6(Trz)_{10}(H_2O)_4[H_2SiW_{12}O_{40}]$, $Na_4H_2[Cu_4(im)_{14}]$-$[Cu_3(H_2O)_3(BiW_9O_{33})_2]$, and $CuSiW_{12}$ have exhibited excellent peroxidase-like activities because of the enhanced stability and the synergistic effect between POMs and MOFs.[26−28] A blemish in an otherwise perfect thing is that the poor conductivity of POMOFs lead to the imperfect performance, such as the relatively high limit of detection (LOD). On the other hand, polypyrrole (PPy), as a typical and common conductive polymer with a large specific surface area, which can provide quick electron transportation such as a bridge, is suited for the enhancement of catalytic performance of materials.[29] In addition, the process of polymerization of PPy is relatively balmy, which cannot destroy the basic structure of host materials.[30−32] On this occasion, PPy has been loaded on the surface of many materials adopting a facile process for performance advancement.[33,34] A case in point is that our group has developed a $AgFKZSiW_{12}$@PPy-based colorimetric biosensing platform with enhanced performance toward $H_2O_2$ and ascorbic acid (AA) detection.[35] However, PPy-based colorimetric biosensors are still limited to the PPy nanoparticle,[36] PPy/hemin nanocomposite,[37] and algae-like $MoS_2$/PPy nanocomposite[38] for the detection of $H_2O_2$ and glucose, but not used toward the detection of UA. This situation urgently motivates us to expand this family toward UA detection for the first time.

As we know, helical structures as the genetic code foundation are ubiquitous in nature, which have gained abundant interest in coordination and material chemistry.[39−42] Because of the vital role of helical structures in biosystems, we guess POMOFs with helicity are a suitable choice for biosensing materials with high structural stability, excellent performance, and good biocompatibility. Inspired by the abovementioned considerations, we plan to assemble helical POMOFs by utilizing Keggin-type POMs, Ag ions, and the 3,5-bis((1*H*-imidazol-1-yl)methyl)-1*H*-1,2,4-triazole (Hbimt) ligand because of the following three reasons: (1) Keggin-type POMs have potential abundance of oxygen atoms to guarantee numerous covalent coordination and flexible steric orientations. (2) Soft multielectron-donating Hbimt ligands possess less steric hindrance and a flexible coordination mode to support the multiple helix fabrication. (3) The $d^{10}$ Ag ions can support numerous coordination numbers to guarantee coordination opportunity with other components. Herein, we synthesized Hbimt ligands successfully according to the literature[43] and prepared a new POM-based fourfold helical MOFs $Ag_5[bimt]_2[PMo_{12}O_{40}]\cdot 2H_2O$ ($Ag_5PMo_{12}$) and then fabricated the stable $Ag_5PMo_{12}$@PPy composite by loading PPy on the $Ag_5PMo_{12}$ surface through an easy oxidative polymerization strategy. The peroxidase-like activity evaluation was systematically performed, indicating that the loading of PPy on the $Ag_5PMo_{12}$ surface indeed improved the peroxidase-like activity effectively because of the synergistic effect. In addition, the colorimetric detection of UA with $Ag_5PMo_{12}$@PPy as peroxidase mimics in the absence of uricase was evaluated in detail (Scheme 1), and the developed sensor was successfully adopted for the UA level determination in human fluids, demonstrating vast future potential ability in clinical and biotechnological applications.

## EXPERIMENTAL SECTION

**Materials and Chemicals.** All chemical reagents of analytical reagent grade were commercially obtained and were directly used in the absence of any additional purification. The ligand (Hbimt) was prepared according to the literature.[43] $H_3PMo_{12}O_{40}$, $AgNO_3$, TMB, UA, $NaH_2PO_4$, $Na_2HPO_4$, AA, urea, triglyceride (Trig), cholesterol (Chol), and glucose (Glu) were obtained from Sinopharm Chemical Reagent Co., Ltd. (Shanghai, China). $CaCO_3$, $MgSO_4$, and $Na_2CO_3$ were provided by Aladdin Chemical Reagent Co., Ltd. (Shanghai, China). $NaVO_3$, 30% $H_2O_2$, NaAc, HAc, HCl, KCl, and $NH_4Cl$ were obtained from Kaitong Chemical Reagent Co., Ltd. (Tianjin, China). Deionized water was utilized throughout the whole experiment.

**Synthesis of $Ag_5[bimt]_2[PMo_{12}O_{40}]\cdot 2H_2O$ ($Ag_5PMo_{12}$).** $H_3PMo_{12}O_{40}$ (120 mg, 0.066 mmol), silver nitrate (85 mg, 0.50 mmol), Hbimt (122 mg, 0.53 mmol), and $NaVO_3$ (36 mg, 0.30 mmol) were dissolved in 8 mL of $H_2O$ and stirred for 0.5 h until homogeneous; then, the pH was regulated to 1.75 approximately with 1 M $HNO_3$, and the mixture was poured into a stainless steel autoclave with Teflon liner (25 mL), which was heated with autogenic


https://dx.doi.org/10.1021/acsbiomaterials.9b01922
ACS Biomater. Sci. Eng. 2020, 6, 1438−1448

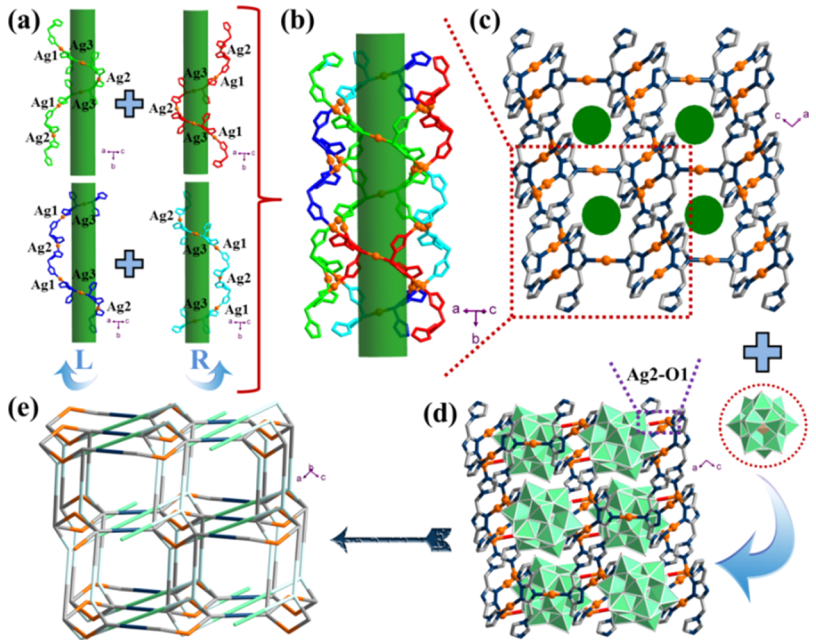


**Figure 1.** Combined ball and stick view of the left- and right-handed helical chains (a) and the one-dimensional quadrilateral channels formed by fourfold helical chains (b) in $Ag_5PMo_{12}$; the three-dimensional MOF in $Ag_5PMo_{12}$ (c); combined polyhedral/ball/stick (d) and topological (e) representation of the POM-encapsulated helical MOF (in the topology, the orange nodes represent Ag1, the dark teal nodes represent Ag3, the light green nodes represent $PMo_{12}$, the light turquoise nodes represent Ag2, and the gray nodes represent the L).

pressure (170 °C, 4 days). After that, reddish brown rhombic crystals (see Figure S1) were obtained by the process of filtration, thorough deionized water washing, and natural drying (yield: 47%, based on Mo). Elemental analysis (EA): $Ag_5C_{20}N_{14}H_{24}O_{42}PMo_{12}$ (2854.07). Calculated: C, 8.42; H, 0.85; N, 6.87 (%). Measured: C, 8.39; H, 0.92; N, 6.84 (%).

**Preparation of $Ag_5PMo_{12}$@PPy and Pure PPy.** First, pyrrole (Py, 50 $\mu$L) was dispersed in deionized water (10 mL). Then, $Ag_5PMo_{12}$ after grinding (500 mg) was added and stirred for 30 min. Finally, 10 mL of $FeCl_3$ solution (10 mg $mL^{-1}$) as the oxidant was added into the obtained mixture dropwise, stirred for 12 h, and kept undisturbed for 8 h under room temperature. The black precipitate was collected by the process of centrifugation and subsequent water and alcohol rinsing and dried using an oven (60 °C, 24 h); then, the resulting product $Ag_5PMo_{12}$@PPy was obtained. The pure PPy was also prepared adopting a procedure similar to that used in $Ag_5PMo_{12}$@PPy without the addition of $Ag_5PMo_{12}$.

**X-ray Crystallographic Measurement and Analysis of $Ag_5PMo_{12}$.** The crystallographic data of $Ag_5PMo_{12}$ were measured and obtained by single-crystal X-ray diffraction on a SMART CCD diffractometer (Bruker, Germany) with Mo K$\alpha$ radiation (graphite monochromatic, $\lambda$: 0.71073 Å). The structure was analyzed with direct methods adopting the SHELXL program[44] and refined using the full matrix least square method on $F^2$. All non H atoms were refined by anisotropic correction, and the locations of H atoms on C atoms were calculated theoretically. Then, the SADABS program was applied for semiempirical absorption corrections. The crystallographic data and the corresponding refinement parameters of $Ag_5PMo_{12}$ were provided (see Table S3). Moreover, some selected bond lengths and angles of $Ag_5PMo_{12}$ were given (see Table S5).

**Characterization of the As-Prepared Samples.** Elemental analyses (EA) were obtained on a PerkinElmer 2400 CHN elemental analyzer (PerkinElmer, USA). The IR spectra were collected on an Alpha Centauri FT-IR spectrometer (Thermo Nicolet, USA) using the KBr pellet ranging from 4000 to 400 $cm^{-1}$. Powder X-ray diffraction (PXRD) patterns were obtained on a MiniFlex600 X-ray diffractometer (Rigaku, Japan) using Cu K$\alpha$ radiation (graphite monochromatic, $\lambda$: 0.154 nm, 2$\theta$: 5−50°). The scanning electron microscopy (SEM) and the corresponding energy-dispersive X-ray (EDX) measurements were performed on Phenom ProX equipment (Phenom, Netherlands; accelerating voltage: 15 kV). X-ray photoelectron spectroscopy (XPS) was performed on a K-Alpha scanning X-ray microprobe (Thermo Scientific, USA) using Al K$\alpha$ radiation.

**Peroxidase-Like Activity Evaluation of $Ag_5PMo_{12}$@PPy.** In order to evaluate the peroxidase-like activity of $Ag_5PMo_{12}$@PPy, the catalytic oxidation reaction of TMB mediated with $H_2O_2$ was performed. In a typical experiment, 200 $\mu$L of $Ag_5PMo_{12}$@PPy dispersion solution (0.6 mg $mL^{-1}$) was added into the mixture of 3 mL of acetate buffer (pH 3.5), 2 mL of 300 $\mu$M TMB (ethanol solution), and 100 $\mu$L of 200 $\mu$M $H_2O_2$; then, the obtained mixture was shaken and incubated in a water bath (40 °C, 10 min). Then, it was filtered with a syringe filter immediately and transferred immediately into a quartz cuvette (1 cm) for the absorbance monitoring by the time scan mode on a T9 UV−vis spectrophotometer (661 nm, Persee, China).

**UA Colorimetric Detection Using $Ag_5PMo_{12}$@PPy.** For UA colorimetric detection, UA solutions with various concentrations were prepared first. Then, 200 $\mu$L of $Ag_5PMo_{12}$@PPy dispersion solution (0.6 mg $mL^{-1}$), 3 mL of acetate buffer (pH = 3.5), 2 mL of 300 $\mu$M TMB, 100 $\mu$L of 200 $\mu$M $H_2O_2$, and 100 $\mu$L of UA solution with a certain concentration were mixed, which were shaken and incubated in a water bath (40 °C, 10 min). Finally, the mixed solution was filtered immediately with a syringe filter and monitored using a UV−vis spectrometer directly at 661 nm.

To carry out the selectivity of $Ag_5PMo_{12}$@PPy in UA detection, various potential interfering substances coexisting in real samples, including UA, AA, urea, triglyceride (Trig), cholesterol (Chol), glucose (Glu), $Mg^{2+}$, $Ca^{2+}$, $NH_4^+$, $Na^+$, $Cl^-$, and $K^+$ were prepared, respectively. The concentration of UA, AA, and urea was 100 $\mu$M, and the concentration of other substances was 500 $\mu$M. Two different experiments were carried out: (1) to test the TMB absorbance in the presence of several interferences individually and (2) to test the TMB absorbance in the copresence of UA and interfering substances. All experiments were carried out with the optimum conditions.

For UA determination in human fluids (serum and urine), the samples (obtained from the Jining People's Hospital, Shandong province) were first dealed with centrifugation (12,000 rpm, 0.5 h) to eliminate the protein species and then the supernatants were collected and diluted (serum: 20-fold, urine: 100-fold) with 100 mM phosphate buffer (pH = 8.5) for the next-step assay as mentioned above.


https://dx.doi.org/10.1021/acsbiomaterials.9b01922
ACS Biomater. Sci. Eng. 2020, 6, 1438−1448

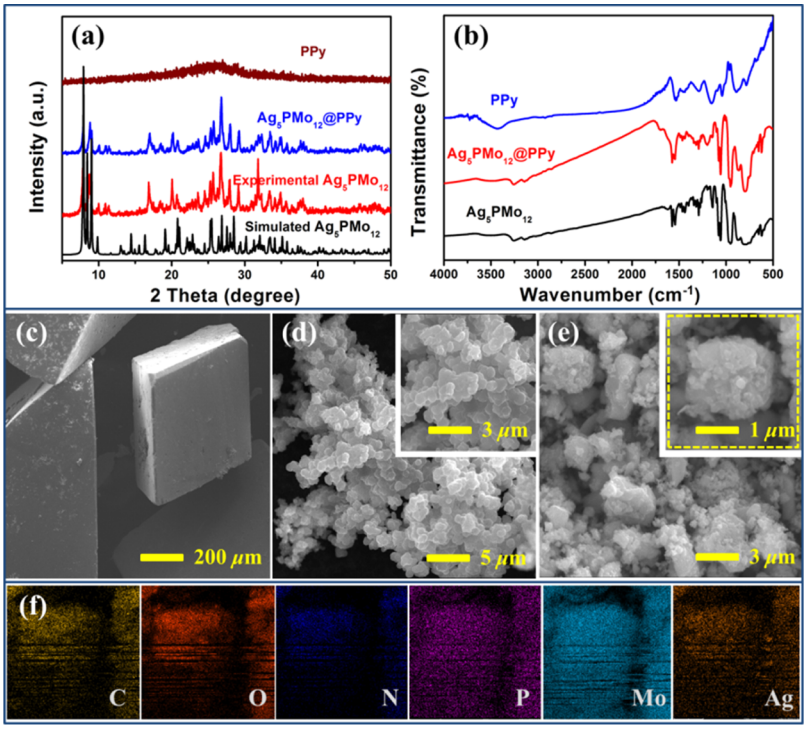


**Figure 2.** PXRD patterns (a) and IR spectra (b) of $Ag_5PMo_{12}$, PPy, and $Ag_5PMo_{12}$@PPy; SEM of $Ag_5PMo_{12}$ (c), PPy (d), and $Ag_5PMo_{12}$@PPy (e), and corresponding EDX elemental mapping images of $Ag_5PMo_{12}$@PPy (f).

## RESULTS AND DISCUSSION

**Structural Description of $Ag_5PMo_{12}$.** Single-crystal X-ray crystallography indicates that $Ag_5PMo_{12}$ crystallizes in monoclinic $P2_1/n$ and the fundamental unit is composed of a half Keggin $PMo_{12}$ polyanion, three crystallographically independent silver ions, a bimt ligand (denoted as L), and free water (Figure S2a). The results of bond valence sum calculations[45] confirm the highest valence states of all Mo(+VI) and Ag(+I) (Table S4). There are three crystallographically independent silver ions company with two distinct coordination modes. In turn, the $PMo_{12}$ polyanions adopt a bi-coordinated mode achieved with two Ag ions (Figure S2b,c). On the other hand, L in $Ag_5PMo_{12}$ all adopt the fully coordination mode achieved with five Ag ions (Figure S2d). Moreover, the bond lengths and angles around silver ions range from 2.101 to 2.145 Å for Ag−N bonds, 2.504 Å for Ag−O bonds, and 165.84−180.05° for N−Ag−N, respectively.

In general, $Ag_5PMo_{12}$ shows an attractive 3D POM-encapsulated fourfold helical MOF. More specifically, the L and Ag ions are connected alternately via two kinds of routes (L-Ag2-L-Ag1-L-Ag3-L-Ag2-L-Ag2-L-Ag1-L-Ag3-L and L-Ag2-L-Ag3-L-Ag1-L-Ag2-L-Ag2-L-Ag3-L-Ag1-L), forming four left- and right-handed helical chains (Figure 1a). Then, fourfold helical chains are interlaced and enclosed perfectly by sharing the L and Ag ions, giving birth to one-dimensional quadrilateral channels (Figure 1b). As a consequence, the vicinal identical quadrilateral channels are elaborately fused together via sharing edges, fabricating a three-dimensional MOF in the view along the *b* axis (Figure 1c). Based on whether the factor of the size of channels is large enough, the $PMo_{12}$ polyanions as guests were encapsulated into the channels through the Ag−O bonds (Ag2−O1), generating a three-dimensional POM-encapsulated helical MOF (Figure 1d). What is interesting and worth noting in the structure is that this packing mode can reduce the contrary charged molecular repulsion and stabilize the overall skeleton. Finally, TOPOS40 software was used for topological analysis, regarding Ag1, Ag3, and $PMo_{12}$ polyanions all as two-connected nodes, Ag2 as three-connected nodes, while the L as five-connected nodes; then, the overall hybrid skeleton can be simplified to a special (2,3,5)-connected net with the point symbol of $\{10\}\{8\cdot10\cdot12\}\{8^4\cdot10^2\cdot12^4\}\{8\}$ (Figure 1e).

**Characterization of the As-Prepared Samples.** As depicted in Figure 2a, the simulated and measured PXRD diffraction patterns of $Ag_5PMo_{12}$ coincide well, confirming the good phase purity. For $Ag_5PMo_{12}$@PPy, the PXRD pattern is similar to that of $Ag_5PMo_{12}$, indicating that the basic framework of $Ag_5PMo_{12}$ is persisted well in the Py polymerization process. In addition, the peaks of PPy are weak in $Ag_5PMo_{12}$@PPy, maybe because of the too small amount of PPy. As depicted in Figure 2b, IR spectra of $Ag_5PMo_{12}$ show four characteristic peaks (1060, 961, 875, and 796 $cm^{-1}$) corresponding to $\nu_{as}$(P−O), $\nu_{as}$(Mo−$O_d$), $\nu_{as}$(Mo−$O_b$−Mo), and $\nu_{as}$(Mo−$O_c$−Mo), respectively. In comparison, the corresponding peaks in $Ag_5PMo_{12}$@PPy changed considerably, indicating slight electron distribution variations in $Ag_5PMo_{12}$ because of the strengthened electrostatic interaction between $Ag_5PMo_{12}$ and PPy. The characteristic peaks situated at 1040, 1397, and 1547 $cm^{-1}$ in $Ag_5PMo_{12}$@PPy are attributed to the Py stretching vibrations, confirming the successful introduction of PPy. Moreover, the SEM technique was employed to inspect the morphologies of PPy, $Ag_5PMo_{12}$, and $Ag_5PMo_{12}$@PPy (Figure 2c−e). It can be observed clearly that $Ag_5PMo_{12}$ shows a clean and smooth surface, but $Ag_5PMo_{12}$@PPy exhibits a coarse surface, indicating that PPy has been loaded on the $Ag_5PMo_{12}$ surface successfully. As shown in Figures S3 and S4, the EDX spectrum and corresponding elemental mapping images in $Ag_5PMo_{12}$ confirm the distribution of C, O, P, Mo,


https://dx.doi.org/10.1021/acsbiomaterials.9b01922
ACS Biomater. Sci. Eng. 2020, 6, 1438−1448

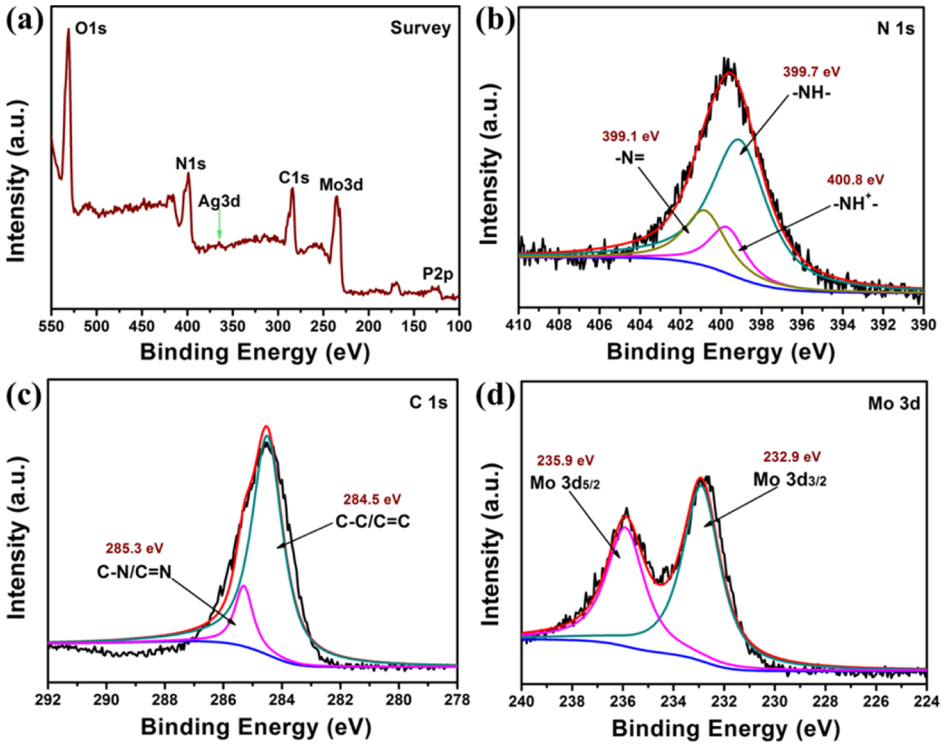


**Figure 3.** XPS spectra of $Ag_5PMo_{12}$@PPy: (a) survey, (b) N 1s, (c) C 1s, and (d) Mo 3d.

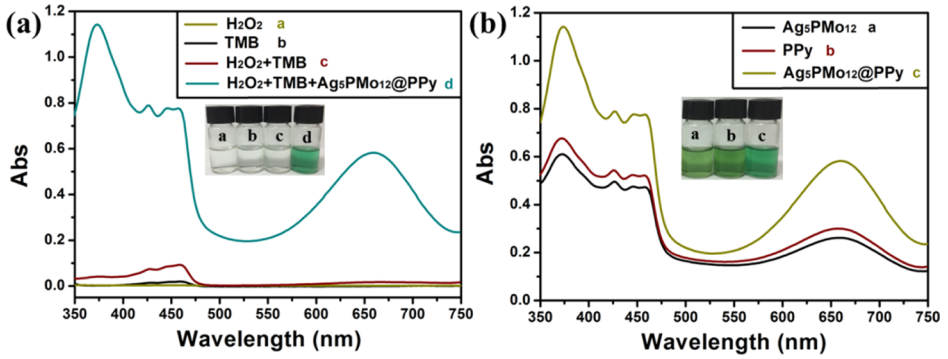


**Figure 4.** (a) UV−vis absorption spectra of $Ag_5PMo_{12}$@PPy-catalyzed TMB color reaction and other control experiments. (b) UV−vis absorption spectra of the $Ag_5PMo_{12}$@PPy-, $Ag_5PMo_{12}$-, and PPy-catalyzed TMB colorimetric system. Typical reaction conditions: acetate buffer (pH 3.5), TMB 300 $\mu$M, and $H_2O_2$ 200 $\mu$M at 40 °C. The inset shows the corresponding digital images.

Ag, and N homogenously. The EDX elemental mapping images of $Ag_5PMo_{12}$@PPy also indicate that the elements C, O, P, Mo, Ag, and N distribute homogeneously (Figures 2f and S5) and the C and N contents of $Ag_5PMo_{12}$@PPy raise obviously than that of $Ag_5PMo_{12}$, further indicating the successful coating of PPy on $Ag_5PMo_{12}$.

As shown in Figure 3a, the XPS spectrum has been applied for $Ag_5PMo_{12}$@PPy analysis, demonstrating the co-existence of O, N, Ag, C, Mo, and P elements. The N 1s spectra could be divided into three peaks (399.1, 399.7, and 400.8 eV), which is attributed to the −N═ and −NH− segments in the PPy chain skeleton and the protonation states of $-NH^+-$, confirming the successful fabrication of PPy (Figure 3b). Two Gaussian peaks belong to the C−C/C═C and C−N/C═N (284.5 and 285.3 eV) and appear in C 1s spectra (Figure 3c). In addition, two main peaks at the binding of 235.9 and 232.9 eV may attribute to $Mo^{6+}$ $3d_{5/2}$ and $Mo^{6+}$ $3d_{3/2}$ appeared in Mo 3d spectra, demonstrating the existence of $Mo^{6+}$ clearly (Figure 3d). These results further verify the successful preparation of $Ag_5PMo_{12}$@PPy.

In order to test the stability, the as-prepared $Ag_5PMo_{12}$ was soaked in HCl (pH = 2) or NaOH (pH = 10) solution. After 24 h, it can be seen that $Ag_5PMo_{12}$ still retains the crystalline state and the solution color is the same as its initial state. Comparing the PXRD patterns and IR spectra of $Ag_5PMo_{12}$ after and before the soaking, it is observed that no significant change appeared except the peak intensity, confirming the outstanding stability toward the pH value (see Figure S6). Owing to the special helical structures and the hydrothermal synthetic approach in acidic conditions, $Ag_5PMo_{12}$ exhibits excellent stability in distinct acidic and basic conditions and in boiling water. The excellent chemical stability is beneficial for fabricating excellent peroxidase mimics for colorimetric biosensors and studying the corresponding peroxidase-like activity.


https://dx.doi.org/10.1021/acsbiomaterials.9b01922
ACS Biomater. Sci. Eng. 2020, 6, 1438−1448

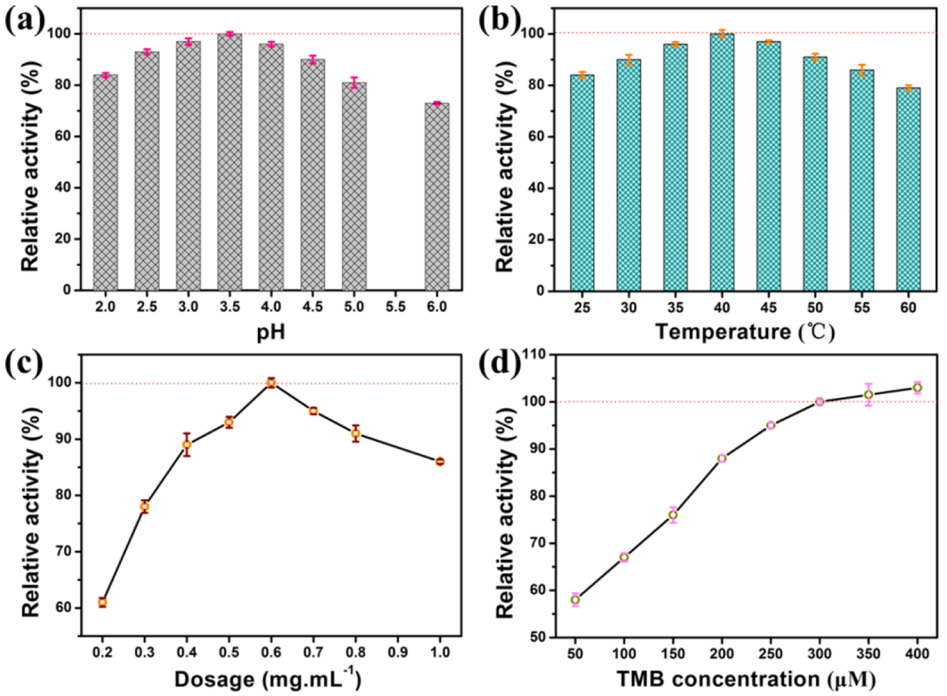


**Figure 5.** Relative activity of $Ag_5PMo_{12}$@PPy under the conditions of different (a) pH values, (b) temperatures, (c) $Ag_5PMo_{12}$@PPy dosages, and (d) TMB concentrations.

**Peroxidase-Like Activity and the Corresponding Mechanism of $Ag_5PMo_{12}$@PPy.** Based on some reported POMOFs and PPy-based nanocomposites having satisfactory peroxidase-like activity,[36] the peroxidase-like activity of fabricated $Ag_5PMo_{12}$@PPy was deeply studied by the TMB catalytic oxidation reaction in the presence of $H_2O_2$ and monitored quantitatively using the UV−vis spectrum. As shown in Figure 4a, a characteristic absorbance at 661 nm corresponding to oxTMB can be seen obviously, and a noticeable solution color change (colorless to green) can be seen effortlessly through bare eyes, indicating that the integrated $Ag_5PMo_{12}$@PPy could induce the TMB color reaction with the presence of $H_2O_2$. The reaction is widely known as the catalytic oxidation of colorless TMB with $^{\bullet}OH$ from the decomposition of $H_2O_2$ into green oxTMB. Conversely, for the control experiments performed under similar conditions, when either TMB, $H_2O_2$, or $Ag_5PMo_{12}$@PPy is absent, no color reaction is achieved and no absorbance appears in the range of 500−750 nm. These results demonstrate that the $Ag_5PMo_{12}$@PPy indeed possesses peroxidase-like activity.

In comparison with $Ag_5PMo_{12}$@PPy, the prepared $Ag_5PMo_{12}$ and PPy exhibit lower activity to trigger the typical reaction. As shown in Figure 4b, the color of $Ag_5PMo_{12}$ and PPy-induced solution is much lighter than that of $Ag_5PMo_{12}$@PPy; meanwhile, the characteristic absorbance intensity at 661 nm of the former two is much deeper than the later one. These results indicate the enhanced peroxidase-like activity of $Ag_5PMo_{12}$@PPy, maybe plausibly owing to the synergistic effect from the integration of PPy and $Ag_5PMo_{12}$. Therefore $Ag_5PMo_{12}$@PPy could be employed as excellent peroxidase mimics.

In general, the mechanism of peroxidase and peroxidase mimics could be divided into two types: the process of electron transfer and the formation of active $^{\bullet}OH$.[46] To confirm the mechanism of $Ag_5PMo_{12}$@PPy, FL tests were performed for the detection of $^{\bullet}OH$ in the reaction. Terephthalic acid was selected as the FL probe for $^{\bullet}OH$ tracking because it could react with $^{\bullet}OH$ and form the 2-hydroxyterephthalic acid product with noticeable FL at 433 nm (Figure S7a). As shown in Figure S7b, it is obvious that the FL intensity in the presence of $Ag_5PMo_{12}$@PPy was far higher than the negligible FL intensity without $Ag_5PMo_{12}$@PPy. This result indicates that $Ag_5PMo_{12}$@PPy can trigger $H_2O_2$ decomposition to form $^{\bullet}OH$ catalytically and result in the oxidation of TMB more efficiently.

**Optimization of Reaction Conditions.** Like the natural peroxidase enzyme and reported peroxidase mimics,[48] the activity of $Ag_5PMo_{12}$@PPy peroxidase mimics is also influenced by reaction conditions. As shown in Figure 5, the relative activity is selected as a standard for the optimization of reaction conditions of the system, and the relevant parameters including the pH, temperature, dosage of peroxidase mimics, and concentration of the substance (TMB and $H_2O_2$) are investigated systematically. The pH influence on the activity of $Ag_5PMo_{12}$@PPy is investigated from 2.0 to 6.0. As provided in Figure 5a, relative activity increases gradually with pH from 2.0 to 3.5 and then decreases with the further pH increase, maybe owing to the affinity decrease of $Ag_5PMo_{12}$@PPy toward substances. Thus, an optimized pH of 3.5 is chosen for further investigation. The temperature influence is studied in the range of 25−60 °C (see Figure 5b). It is observed that excessive high or low temperature is adverse for the reaction, and reaction temperature fixed at 40 °C is found to provide the maximum of relative activity. The effect of the $Ag_5PMo_{12}$@PPy dosage is investigated from 0.2 to 1.0 mg $mL^{-1}$ (Figure 5c). Relative activity increases with the dosage increase of $Ag_5PMo_{12}$@PPy up to 0.6 mg $mL^{-1}$, above which it decreases gradually. The result indicates that the activity of the system is highly dependent on the dosage of $Ag_5PMo_{12}$@PPy, which needs to be well controlled. Therefore, 0.6 mg $mL^{-1}$ $Ag_5PMo_{12}$@PPy is selected in the subsequent assays. TMB is the main substrate,


https://dx.doi.org/10.1021/acsbiomaterials.9b01922
ACS Biomater. Sci. Eng. 2020, 6, 1438−1448

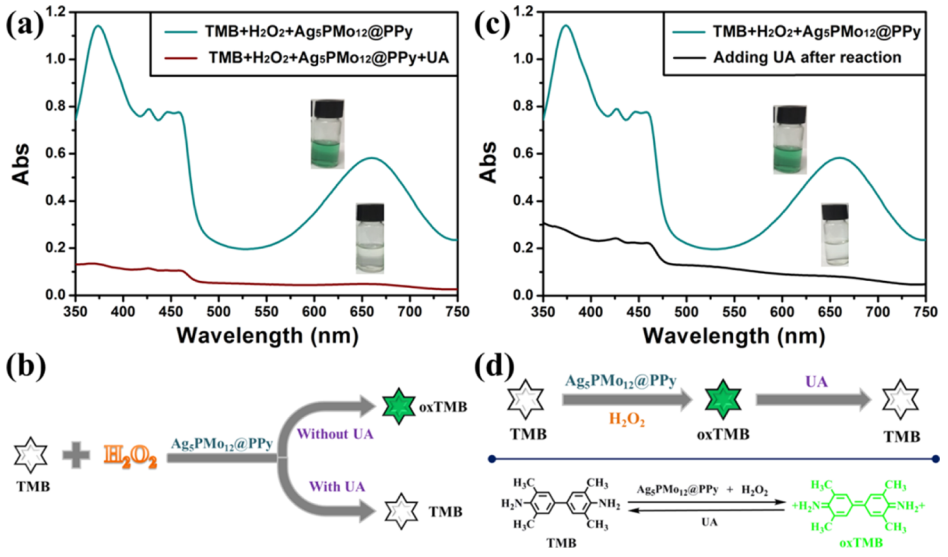


**Figure 6.** (a) Absorption spectra of the $H_2O_2$ + TMB + $Ag_5PMo_{12}$@PPy system simultaneously added UA or not and (b) the corresponding process. (c) Absorption spectra of the $H_2O_2$ + TMB + $Ag_5PMo_{12}$@PPy system with or without the addition of UA after the reaction and (d) the corresponding process.

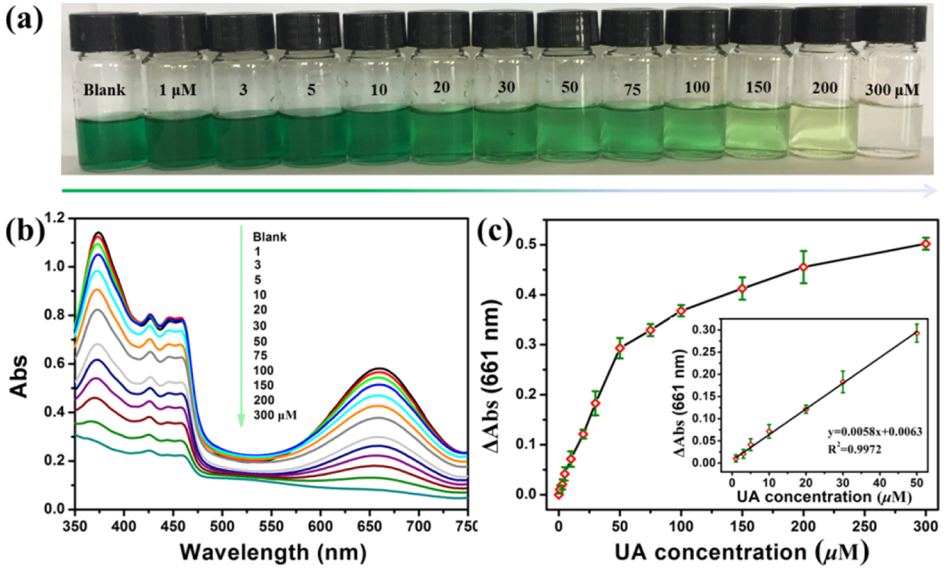


**Figure 7.** (a) Photographs and (b) UV−vis spectra of the $Ag_5PMo_{12}$@PPy-based biosensor with the presence of different UA doses (up to down: 0, 1, 3, 5, 10, 20, 30, 50, 75, 100, 150, 200, and 300 $\mu$M). (c) Response curve of the $\Delta A$661 nm signal as a function of UA concentration with first-best conditions (inset: linear regression curve). The error bars: the standard deviations of three repeated tests.

and the concentration of it can directly influence the system activity. Thus, the effect of the TMB concentration (50−400 $\mu$M) on activity is also studied (Figure 5d). It is observed that the relative activity increases gradually with the increase of TMB concentration, and when the concentration of TMB is higher than 300 $\mu$M, it reaches a dynamic equilibrium. Accordingly, 300 $\mu$M is selected as the first-best TMB concentration. In addition, we test the activity of $Ag_5PMo_{12}$@PPy against the $H_2O_2$ concentration, and the result confirms that the best peroxidase-like activity is achieved at 200 $\mu$M. Beyond this value, the activity instead declines gradually with the increase of concentration. Thus, 200 $\mu$M is determined as the optimal $H_2O_2$ concentration (Figure S8).

**Steady State Kinetics Experiments of $Ag_5PMo_{12}$@PPy.** As we all know, the smaller $K_m$ value indicates the stronger affinity of the peroxidase mimics ($Ag_5PMo_{12}$@PPy) with the substrates ($H_2O_2$ and TMB). Herein, in Figure S9 and Table S2, the $K_m$ values of $Ag_5PMo_{12}$@PPy with $H_2O_2$ and TMB as substrates are 0.246 and 0.034 mM, respectively, both lower than those of the most reported peroxidase mimics (e.g., MOF-808 and $AgFKZSiW_{12}$), confirming that $Ag_5PMo_{12}$@PPy has higher binding affinity with substrates. Meanwhile, the $V_{max}$ values of $Ag_5PMo_{12}$@PPy with $H_2O_2$ and TMB as substrates are both higher than those of most reported peroxidase mimics (e.g., PPy), demonstrating that $Ag_5PMo_{12}$@PPy has higher affinity with substrates and better catalytic efficiency than most reported peroxidase mimics. These results are consistent with the excellent peroxidase-like activity of $Ag_5PMo_{12}$@PPy.

**Mechanism of the $Ag_5PMo_{12}$@PPy-Catalyzed Reaction Inhibited with UA.** It is observed that UA could inhibit $Ag_5PMo_{12}$@PPy-catalyzed TMB color reaction. As depicted in Figure 6a, a remarkable solution color change (colorless to


https://dx.doi.org/10.1021/acsbiomaterials.9b01922
ACS Biomater. Sci. Eng. 2020, 6, 1438−1448

green) is observed in the $Ag_5PMo_{12}$@PPy-catalyzed reaction system. When $H_2O_2$, TMB, $Ag_5PMo_{12}$@PPy, and UA are added into the acetate buffer simultaneously, the change of color is invisible, revealing that UA can inhibit the TMB color reaction (the process is given in Figure 6b). Three fundamental mechanisms for the inhibition of UA toward the TMB color reaction have been deduced: (i) based on the activity of mimics which is highly dependent on the surface properties,[48] the additive UA maybe adsorbed on the surface of $Ag_5PMo_{12}$@PPy and suppresses the peroxidase-like activity. (ii) UA may consume the $^{\bullet}OH$ from the decomposition of $H_2O_2$, therefore hindering the oxidation reaction of TMB. (iii) UA may possess the reduce ability to induce green oxTMB to colorless TMB again. In order to further indicate the real mechanism, we perform another experiment. $H_2O_2$, TMB, and $Ag_5PMo_{12}$@PPy are added into the buffer for the activation of TMB color reaction first, and when a green color occurred in 10 min, UA is added. As shown in Figure 6c,d, the added UA induces solution fading, revealing that the inhibition of the TMB color reaction is originated from the green oxTMB reducing to colorless TMB again through additive UA.

**Colorimetric Sensing of UA Using $Ag_5PMo_{12}$@PPy.** According to the abovementioned finding, under the optimized reaction conditions, a new uricase-free biosensor has been obtained for UA colorimetric sensing. This device is based on the inhibition of the TMB color reaction (appears easily with the presence of $Ag_5PMo_{12}$@PPy and $H_2O_2$) by UA selectively. As depicted in Figure 7a,b, along with the target UA concentration increasing, the absorption peak decreases remarkably and the dark green color fades to light green and eventually colorless, which can be visualized easily through bare eyes. Thus, the absorbance change of oxTMB is used in UA level quantitative sensing. Surprisingly, very little UA is able to result in the absorbance decline at 661 nm. Figure 7c exhibits the typical UA dose response curve, indicating that the evaluation standard of $\Delta A$ ($\Delta A = A_0 - A$, where $A_0$ and $A$ mean the oxTMB absorbance at 661 nm on the condition of the blank group and UA with different concentrations, respectively) gradually increases with the increase of UA dose, and the linear regression curve is obtained when the UA dose is up to 50 $\mu$M. Therefore, the good dependence of the absorbance upon the UA dose in the range of 1−50 $\mu$M can be well described by the linear regression formula as $\Delta A = 0.0058C_{UA} + 0.0063$ ($R^2$: 0.9972), providing the sensitivity of 0.0058 $\mu M^{-1}$, which is superior than that of MIL-53(Fe) (0.00239 $\mu M^{-1}$).[49] Based on the $3\sigma$/slope rule, the LOD is found to be 0.47 $\mu$M (inset in Figure 7c). As shown in Table 1, the LOD of UA detection in this work is comparable or even better than that of most reports [e.g., Th-MOF (1.15 $\mu$M) and CoP/NF (1.0 $\mu$M)]. The more interest thing is that this biosensor can run without any natural enzyme (including uricase), which gives excellent reproducibility and stability for the developed device. Finally, the repeatability of this biosensor is tested through five repeated measurements of 50 $\mu$M UA standard solution, leading to a relative standard deviation (RSD) of 1.49% (Figure S10).

**Overall Mechanism of UA Colorimetric Biosensing Based on $Ag_5PMo_{12}$@PPy.** As proposed in Figure 8, during the UA colorimetric biosensing process, the electrons were first excited with $Ag_5PMo_{12}$ and then transferred to PPy, preventing the electron−hole pair recombination effectively. Then, $H_2O_2$ as an electron scavenger was adsorbed on the $Ag_5PMo_{12}$@PPy surface, through the O−O bond break up and the proton and

**Table 1. Comparison of Our Proposed Sensor with Some Reported Assay Systems for UA Detection**

| assay system | linear range ($\mu$M) | LOD ($\mu$M) | real sample | refs |
|---|---|---|---|---|
| uricase/g-$C_3N_4$ | 10−100 | 8.9 | | 12 |
| uricase/$Cu^{2+}$ | 1−100 | 0.64 | urine | 13 |
| uricase/MIL-53(Fe) | 4.5−60 | 1.3 | serum and urine | 49 |
| uricase/Ag nanoprisms | 1−40 | 0.7 | serum | 50 |
| uricase/$ZnFe_2O_4$ MNPs | 10−1000 | 5.79 | serum | 51 |
| uricase/Th-MOF | 4−70 | 1.15 | serum and urine | 52 |
| Ni@$MnO_2$ (without uricase) | 1−40 | 0.24 | serum | 53 |
| CoP/NF (without uricase) | 1−200 | 1.0 | serum and urine | 54 |
| $Ag_5PMo_{12}$@PPy (without uricase) | 1−50 | 0.47 | serum and urine | this work |

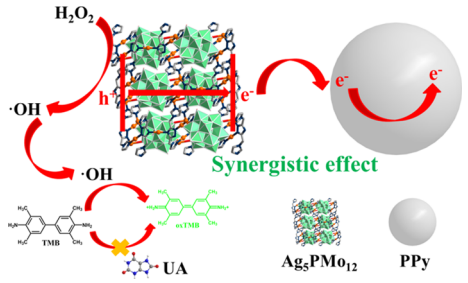


**Figure 8.** Mechanism scheme of the peroxidase-like activity of $Ag_5PMo_{12}$@PPy toward UA colorimetric biosensing.

electron transfer, forming double active $^{\bullet}OH$, which was stabilized with $Ag_5PMo_{12}$@PPy.[55] Subsequently, TMB was adsorbed onto the $Ag_5PMo_{12}$@PPy surface and reacted with desorbed $^{\bullet}OH$ by the process of electron transfer, leading to the TMB catalytic oxidation reaction, in which TMB converted to oxTMB and the corresponding color converted from colorless to green. When UA was added into this system, the catalytic oxidation of TMB was inhibited, leading to no green color formation.

**Recyclability and Stability Study.** The recyclability of peroxidase mimics is a vital aspect in practical application. As depicted in Figure S11, the $\Delta A$661 nm signals of the sensing system in four measurements are recorded utilizing the same recycled $Ag_5PMo_{12}$@PPy after sensing reaction. No huge change of the signals is seen, leading to an RSD of 1.2%. The activity decrease may be originated from the aggregation and loss of $Ag_5PMo_{12}$@PPy during the centrifugation process. This result indicates the excellent recyclability of the obtained $Ag_5PMo_{12}$@PPy enzyme mimics, which is superior than that of MOF-808.[21] As shown in Figures S12 and S13, the PXRD patterns and IR spectra of $Ag_5PMo_{12}$@PPy before and after the reaction show peak position similarity exactly, confirming the ultrahigh stability of $Ag_5PMo_{12}$@PPy as peroxidase-like mimics. Comparing with the previously reported Keggin-type POM-based enzyme mimic, the robustness of $Ag_5PMo_{12}$@PPy makes it a promising material for broad applications in biodetection.

**Interference Evaluation.** In order to evaluate the reasonably expected selectivity of the developed UA colorimetric biosensor, the investigation was performed with the optimal conditions with various substrates commonly co-existing in blood and urine added, including AA, urea,


https://dx.doi.org/10.1021/acsbiomaterials.9b01922
ACS Biomater. Sci. Eng. 2020, 6, 1438−1448

triglyceride (Trig), cholesterol (Chol), glucose (Glu), $Mg^{2+}$, $Ca^{2+}$, $NH_4^+$, $Na^+$, $Cl^-$, and $K^+$. As shown in Figure 9a, the

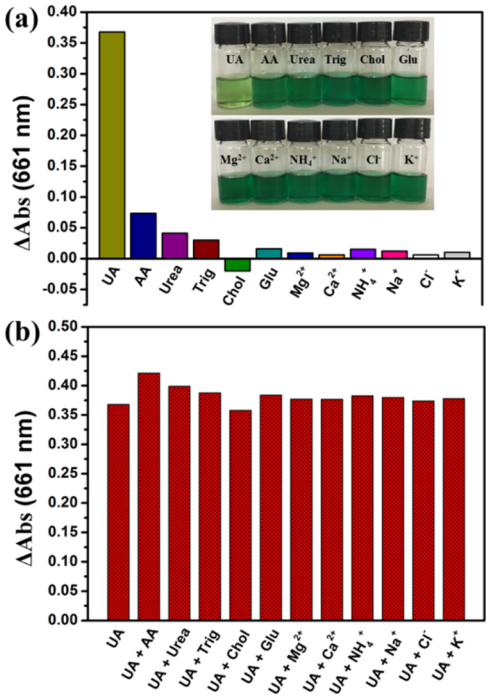


**Figure 9.** Selectivity of the $Ag_5PMo_{12}$@PPy-based biosensor for UA sensing. Each potential interference is added separately (a) without and (b) with UA, and the absorbance at 661 nm is quantitatively measured using UV−vis spectra. Several substances are UA, AA, urea, triglyceride, cholesterol, glucose, $Mg^{2+}$, $Ca^{2+}$, $NH_4^+$, $Na^+$, $Cl^-$, and $K^+$ (from left to right). The dose of UA, AA, and urea is 100 $\mu$M, and the dose of other potential interferences is 500 $\mu$M.

evaluation standard of $\Delta A661$ nm exhibits an obvious increase for UA than other interferences, indicating good selectivity for UA colorimetric sensing. Additionally, the specificity of this UA biosensor was further indicated by pre-mixing potential interferences with UA and then added respectively. As given in Figure 9b, the $\Delta A661$ nm in the copresence of UA and interferences is almost similar to that without interferences, confirming that this biosensor responded specifically toward UA. It is found that the co-existence of interferences have no obvious interference on the UA detection; thus, the proposed biosensor displays good selectivity (comparable with Ni@$MnO_2$),[53] which is appropriate for the reliable point-of-care UA sensing in blood and urine samples after the process of dilution.

**Detection of UA in Human Serum and Urine Samples.** In order to assess the feasibility and practical ability of the fabricated UA sensor, three human serum samples from the hospital were monitored through the proposed method. Considering that the UA level in serum and urine may be higher than the detection range, a dilution process was carried out before tests. Taking the dilution folds into calculation, the results from our biosensor are comparable with the clinical results (see Table 2). For all samples, the data from our biosensor are well-consistent with the clinical data, leading to an average relative error (RE) of 1.52%, providing excellent reliability for UA sensing in human serum samples. In addition, the accuracy test of our fabricated sensor was tested through the addition of UA standard solutions with different doses (0, 10, and 20 $\mu$M) into the serum and urine samples after 20- and 100-fold dilution, respectively. As shown in Table 3, the calculated and recorded recovery values are between 95.0 and 106.1% with the RSD range of 0.85−2.76%. These satisfactory data verify that good practicability and repeatability of our developed colorimetric sensor has been acquired during practical sample measurements.

**Table 2. UA Contents in Human Serum Samples Measured by Our Proposed Colorimetric Sensor and Obtained from the Clinical Data**

| | UA concentration ($\mu$M) | | | |
|---|---|---|---|---|
| samples | clinical data[a,b] | proposed sensor[b] | RE (%)[c] | average RE (%) |
| serum 1 | 203.5 ± 3.5 | 209.8 ± 2.9 | 3.10 | 1.52 |
| serum 2 | 517.3 ± 13.3 | 514.1 ± 6.7 | 0.62 | |
| serum 3 | 386.4 ± 7.8 | 389.6 ± 5.4 | 0.83 | |

[a]Data supported by the Qufu People's Hospital of Shandong province. [b]Each sample was measured three times repeatedly. [c]RE represents the relative error.

**Table 3. Recoveries of UA Detection in Human Serum and Urine Samples by Our Fabricated Colorimetric Biosensor**

| samples | added ($\mu$M) | measured ($\mu$M)[a] | recovery (%) | RSD (%, $n$ = 3) |
|---|---|---|---|---|
| serum 1 | 0 | 10.51 ± 0.19 | | 2.26 |
| | 10 | 20.13 ± 0.26 | 98.1 | 1.64 |
| | 20 | 29.65 ± 0.33 | 97.2 | 1.41 |
| | 0 | 25.70 ± 0.57 | | 2.76 |
| serum 2 | 10 | 33.92 ± 0.33 | 95.0 | 1.32 |
| | 20 | 46.35 ± 0.78 | 101.4 | 2.08 |
| | 0 | 15.78 ± 0.31 | | 2.49 |
| urine 1 | 10 | 26.91 ± 0.23 | 104.4 | 1.06 |
| | 20 | 34.96 ± 0.67 | 97.7 | 2.35 |
| | 0 | 23.53 ± 0.49 | | 2.55 |
| urine 2 | 10 | 35.57 ± 0.24 | 106.1 | 0.85 |
| | 20 | 44.94 ± 0.64 | 103.2 | 1.75 |

[a]Each sample was measured three times repeatedly.

## CONCLUSIONS

In summary, a new composite based on POM-encapsulated fourfold helical MOFs and suited PPy coating ($Ag_5PMo_{12}$@PPy) as a monolithic peroxidase mimic, exhibiting significantly improved peroxidase-like activity owing to the synergistic effect to trigger the TMB color reaction with the participation of $H_2O_2$ has been developed. It is observed surprisingly that the TMB color reaction can be inhibited with UA especially accompanied by bare eye observable color change of the system. Therefore, a novel UA colorimetric biosensor is achieved successfully based on this result. This colorimetric biosensor has no need of any natural peroxidase or uricase, giving outstanding reproducibility and stability toward environments. With the optimal conditions, excellent linear relationship of $\Delta A661$ nm and UA dose ranging from 1 to 50 $\mu$M are obtained with LOD of 0.47 $\mu$M. More significantly, this fabricated biosensor held the application prospect for UA detection in human real samples. These advantages together enable the developed biosensor as a simple and promising device for UA sensing in the field of clinical diagnosis and bioanalysis.


https://dx.doi.org/10.1021/acsbiomaterials.9b01922
ACS Biomater. Sci. Eng. 2020, 6, 1438−1448

## ■ ASSOCIATED CONTENT

### Supporting Information

The Supporting Information is available free of charge at https://pubs.acs.org/doi/10.1021/acsbiomaterials.9b01922.

Crystallographic data and CCDC can be obtained via www.ccdc.cam.ac.uk/data_request/cif.

Crystal data of $Ag_5PMo_{12}$ and supplementary figures and tables(PDF)

## ■ AUTHOR INFORMATION


### Corresponding Author

**Jing-Quan Sha** − *Chemistry and Chemical Engineering Department, Jining University, Qufu, Shandong 273155, China;* orcid.org/0000-0002-5925-9565; Email: shajq2002@126.com

### Authors

**Ying-Ying Wang** − *Chemistry and Chemical Engineering Department, Jining University, Qufu, Shandong 273155, China*

**Hai-Feng Zhang** − *Chemistry and Chemical Engineering Department, Jining University, Qufu, Shandong 273155, China*

**Dong-Hui Wang** − *Chemistry and Chemical Engineering Department, Jining University, Qufu, Shandong 273155, China*

**Ning Sheng** − *Chemistry and Chemical Engineering Department, Jining University, Qufu, Shandong 273155, China*

**Gong-Guo Zhang** − *Chemistry and Chemical Engineering Department, Jining University, Qufu, Shandong 273155, China*

**Ling Yin** − *Chemistry and Chemical Engineering Department, Jining University, Qufu, Shandong 273155, China*

Complete contact information is available at: https://pubs.acs.org/10.1021/acsbiomaterials.9b01922


### Notes

The authors declare no competing financial interest.

## ■ ACKNOWLEDGMENTS

The financial support was achieved from the National Natural Science Foundation of China (21771061), the Project of Higher Educational Science and Technology Program in Shandong Province (J12LD54), the Youths Science Foundation of Jining University (2017BSZX09), and the Talent Culturing Plan for Leading Disciplines in University of Shandong Province (J17KA118).

## ■ REFERENCES


(1) Huang, S.-H.; Shih, Y.-C.; Wu, C.-Y.; Yuan, C.-J.; Yang, Y.-S.; Li, Y.-K.; Wu, T.-K. Detection of serum uric acid using the optical polymeric enzyme biochip system. *Biosens. Bioelectron.* **2004**, *19*, 1627−1633.

(2) Luo, Y.-C.; Do, J.-S.; Liu, C.-C. An amperometric uric acid biosensor based on modified Ir−C electrode. *Biosens. Bioelectron.* **2006**, *22*, 482−488.

(3) Raj, C. R.; Ohsaka, T. Voltammetric detection of uric acid in the presence of ascorbic acid at a gold electrode modified with a self-assembled monolayer of heteroaromatic thiol. *J. Electroanal. Chem.* **2003**, *540*, 69−77.

(4) Falasca, G. F. Metabolic diseases: gout. *Clin. Dermatol.* **2006**, *24*, 498−508.

(5) Nyhan, W. L. Disorders of purine and pyrimidine metabolism. *Mol. Genet. Metab.* **2005**, *86*, 25−33.

(6) Srinivasan, S.; Kalaiselvi, P.; Sakthivel, R.; Pragasam, V.; Muthu, V.; Varalakshmi, P. Uric acid: an abettor or protector in calcium oxalate urolithiasis? Biochemical study in stone formers. *Clin. Chim. Acta* **2005**, *353*, 45−51.

(7) Jen, J.-F.; Hsiao, S.-L.; Liu, K.-H. Simultaneous determination of uric acid and creatinine in urine by an eco-friendly solvent-free high performance liquid chromatographic method. *Talanta* **2002**, *58*, 711−717.

(8) Perello, J.; Sanchis, P.; Grases, F. Determination of uric acid in urine, saliva and calcium oxalate renal calculi by high-performance liquid chromatography/mass spectrometry. *J. Chromatogr. B* **2005**, *824*, 175−180.

(9) Boughton, J. L.; Robinson, B. W.; Strein, T. G. Determination of uric acid in human serum by capillary electrophoresis with polarity reversal and electrochemical detection. *Electrophoresis* **2002**, *23*, 3705−3710.

(10) Galbán, J.; Andreu, Y.; Almenara, M. J.; Marcos, S.; Castillo, J. R. Direct determination of uric acid in serum by a fluorometric-enzymatic method based on uricase. *Talanta* **2001**, *54*, 847−854.

(11) Kumar, A. S.; Shanmugam, R. Simple method for simultaneous detection of uric acid, xanthine and hypoxanthine in fish samples using a glassy carbon electrode modified with as commercially received multiwalled carbon nanotubes. *Anal. Methods* **2011**, *3*, 2088−2094.

(12) Lu, Q.; Deng, J.; Hou, Y.; Wang, H.; Li, H.; Zhang, Y. One-step electrochemical synthesis of ultrathin graphitic carbon nitride nanosheets and their application to the detection of uric acid. *Chem. Commun.* **2015**, *51*, 12251−12253.

(13) Lu, H.-F.; Li, J.-Y.; Zhang, M.-M.; Wu, D.; Zhang, Q.-L. A highly selective and sensitive colorimetric uric acid biosensor based on Cu(II)-catalyzed oxidation of 3,3',5,5'-tetramethylbenzidine. *Sens. Actuators, B* **2017**, *244*, 77−83.

(14) Zhao, H.; Wang, Z.; Jiao, X.; Zhang, L.; Lv, Y. Uricase-Based Highly Sensitive and Selective Spectrophotometric Determination of Uric Acid Using BSA-Stabilized Au Nanoclusters as Artificial Enzyme. *Spectrosc. Lett.* **2012**, *45*, 511−519.

(15) Hill, C. L. Introduction: Polyoxometalates Multicomponent Molecular Vehicles to Probe Fundamental Issues and Practical Problems. *Chem. Rev.* **1998**, *98*, 1−2.

(16) Zheng, S.-T.; Zhang, J.; Li, X.-X.; Fang, W.-H.; Yang, G.-Y. Cubic Polyoxometalate−Organic Molecular Cage. *J. Am. Chem. Soc.* **2010**, *132*, 15102−15103.

(17) Lin, H.; Wang, J.-W.; Guo, X.-W.; Yao, S.; Liu, M.; Zhang, Z.-M.; Lu, T.-B. Phosphorized polyoxometalate-etched iron-hydroxide porous nanotubes for efficient electrocatalytic oxygen evolution. *J. Mater. Chem. A* **2018**, *6*, 24479−24485.

(18) Wang, J.; Han, D.; Wang, X.; Qi, B.; Zhao, M. Polyoxometalates as peroxidase mimetics and their applications in $H_2O_2$ and glucose detection. *Biosens. Bioelectron.* **2012**, *36*, 18−21.

(19) Liu, S.; Tian, J.; Wang, L.; Zhang, Y.; Luo, Y.; Li, H.; Asiri, A. M.; Al-Youbi, A. O.; Sun, X. Fast and Sensitive Colorimetric Detection of $H_2O_2$ and Glucose: A Strategy Based on Polyoxometalate Clusters. *ChemPlusChem* **2012**, *77*, 541−544.

(20) Li, D.; Han, H.; Wang, Y.; Wang, X.; Li, Y.; Wang, E. Modification of Tetranuclear Zirconium-Substituted Polyoxometalates-Syntheses, Structures, and Peroxidase-Like Catalytic Activities. *Eur. J. Inorg. Chem.* **2013**, *2013*, 1926−1934.

(21) Zheng, H.-Q.; Liu, C.-Y.; Zeng, X.-Y.; Chen, J.; Lü, J.; Lin, R.-G.; Cao, R.; Lin, Z.-J.; Su, J.-W. MOF-808: A Metal−Organic Framework with Intrinsic Peroxidase-Like Catalytic Activity at Neutral pH for Colorimetric Biosensing. *Inorg. Chem.* **2018**, *57*, 9096−9104.

(22) Li, S.; Liu, X.; Chai, H.; Huang, Y. Recent advances in the construction and analytical applications of metal-organic frameworks-based nanozymes. *TrAC, Trends Anal. Chem.* **2018**, *105*, 391−403.

(23) Wu, J.; Wang, X.; Wang, Q.; Lou, Z.; Li, S.; Zhu, Y.; Qin, L.; Wei, H. Nanomaterials with enzyme-like characteristics (nanozymes): next-generation artificial enzymes (II). *Chem. Soc. Rev.* **2019**, *48*, 1004−1076.

(24) Song, W.; Zhao, B.; Wang, C.; Ozaki, Y.; Lu, X. Functional nanomaterials with unique enzyme-like characteristics for sensing applications. *J. Mater. Chem. B* **2019**, *7*, 850−875.
(25) Lin, Z.-J.; Zheng, H.-Q.; Chen, J.; Zhuang, W.-E.; Lin, Y.-X.; Su, J.-W.; Huang, Y.-B.; Cao, R. Encapsulation of Phosphotungstic Acid into Metal−Organic Frameworks with Tunable Window Sizes: Screening of PTA@MOF Catalysts for Efficient Oxidative Desulfurization. *Inorg. Chem.* **2018**, *57*, 13009−13019.
(26) Zhou, E.-L.; Qin, C.; Huang, P.; Wang, X.-L.; Chen, W.-C.; Shao, K.-Z.; Su, Z.-M. A Stable Polyoxometalate-Pillared Metal-Organic Framework for Proton-Conducting and Colorimetric Biosensing. *Chem.—Eur. J.* **2015**, *21*, 11894−11898.
(27) Chai, D.-F.; Ma, Z.; Yan, H.; Qiu, Y.; Liu, H.; Guo, H.-D.; Gao, G.-G. Synergistic effect of sandwich polyoxometalates and copper−imidazole complexes for enhancing the peroxidase-like activity. *RSC Adv.* **2015**, *5*, 78771−78779.
(28) Li, X.; Li, S.; Wang, Y.; Zhou, K.; Li, P.; Sha, J. Synthesis, structure and effective peroxidase-like activity of a stable polyoxometalate-pillared metal-organic framework with multinuclear cycles. *Polyhedron* **2018**, *151*, 206−212.
(29) Chowdhury, D.; Paul, A.; Chattopadhyay, A. Photocatalytic Polypyrrole-$TiO_2$-Nanoparticles Composite Thin Film Generated at the Air−Water Interface. *Langmuir* **2005**, *21*, 4123−4128.
(30) Li, Q.; Zhang, C.; Li, J. Photocatalytic and microwave absorbing properties of polypyrrole/Fe-doped $TiO_2$ composite by in situ polymerization method. *J. Alloys Compd.* **2011**, *509*, 1953−1957.
(31) Wang, D.; Wang, Y.; Li, X.; Luo, Q.; An, J.; Yue, J. Sunlight photocatalytic activity of polypyrrole−$TiO_2$ nanocomposites prepared by 'in situ' method. *Catal. Commun.* **2008**, *9*, 1162−1166.
(32) Jin, B.; Gao, F.; Zhu, Y.-F.; Lang, X.-Y.; Han, G.-F.; Gao, W.; Wen, Z.; Zhao, M.; Li, J.-C.; Jiang, Q. Facile Synthesis of Non-Graphitizable Polypyrrole-Derived Carbon/Carbon Nanotubes for Lithium-ion Batteries. *Sci. Rep.* **2016**, *6*, 19317.
(33) Xu, X.; Gao, X.; Lu, T.; Liu, X.; Wang, X. Hybrid material based on a coordination-complex-modified polyoxometalate nanorod (CC/POMNR) and PPy: a new visible light activated and highly efficient photocatalyst. *J. Mater. Chem. A* **2015**, *3*, 198−206.
(34) Ramanaviciene, A.; Ramanavicius, A. Application of Polypyrrole for the Creation of Immunosensors. *Crit. Rev. Anal. Chem.* **2002**, *32*, 245−252.
(35) Li, X.; Sun, L.; Yang, X.; Zhou, K.; Zhang, G.; Tong, Z.; Wang, C.; Sha, J. Enhancing the colorimetric detection of $H_2O_2$ and ascorbic acid on polypyrrole coated fluconazole-functionalized POMOFs. *Analyst* **2019**, *144*, 3347−3356.
(36) Tao, Y.; Ju, E.; Ren, J.; Qu, X. Polypyrrole nanoparticles as promising enzyme mimics for sensitive hydrogen peroxide detection. *Chem. Commun.* **2014**, *50*, 3030−3032.
(37) Hu, P.; Han, L.; Dong, S. A Facile One-Pot Method to Synthesize a Polypyrrole/Hemin Nanocomposite and Its Application in Biosensor, Dye Removal, and Photothermal Therapy. *ACS Appl. Mater. Interfaces* **2014**, *6*, 500−506.
(38) Lei, J.; Lu, X.; Nie, G.; Jiang, Z.; Wang, C. One-Pot Synthesis of Algae-Like $MoS_2$/PPy Nanocomposite: A Synergistic Catalyst with Superior Peroxidase-Like Catalytic Activity for $H_2O_2$ Detection. *Part. Part. Syst. Charact.* **2015**, *32*, 886−892.
(39) Shi, Z.; Feng, S.; Gao, S.; Zhang, L.; Yang, G.; Hua, J. Inorganic-Organic Hybrid Materials Constructed from $[(VO_2)(HPO_4)]_\infty$ Helical Chains and $[M(4,4'\text{-bpy})_2]^{2+}$ (M=Co, Ni) Fragments. *Angew. Chem., Int. Ed.* **2000**, *39*, 2325−2327.
(40) Cui, Y.; Lee, S. J.; Lin, W. Interlocked Chiral Nanotubes Assembled from Quintuple Helices. *J. Am. Chem. Soc.* **2003**, *125*, 6014−6015.
(41) Jiang, H.-L.; Liu, B.; Xu, Q. Rational Assembly of $d^{10}$ Metal−Organic Frameworks with Helical Nanochannels Based on Flexible V-Shaped Ligand. *Cryst. Growth Des.* **2010**, *10*, 806−811.
(42) Han, L.; Hong, M.; Wang, R.; Luo, J.; Lin, Z.; Yuan, D. A novel nonlinear optically active tubular coordination network based on two distinct homo-chiral helices. *Chem. Commun.* **2003**, 2580−2581.
(43) Alcalde, E.; Alemany, M.; Gisbert, M.; Pérez-García, L. Synthesis of quadrupolar [14] heterocycles built up from heterocyclic betaine subunits. *Synlett* **1995**, *1995*, 757−760.
(44) Sheldrick, G. *SHELX-97, Program for Crystal Structure Refinement*; University of Göttingen: Germany, 1997.
(45) Brown, I. D.; Altermatt, D. Bond-valence parameters obtained from a systematic analysis of the Inorganic Crystal Structure Database. *Acta Crystallogr., Sect. B: Struct. Sci.* **1985**, *41*, 244−247.
(46) Liu, B.; Liu, J. Surface modification of nanozymes. *Nano Res.* **2017**, *10*, 1125−1148.
(47) Sun, H.; Zhou, Y.; Ren, J.; Qu, X. Carbon Nanozymes: Enzymatic Properties, Catalytic Mechanism and Applications. *Angew. Chem., Int. Ed.* **2018**, *57*, 9224−9237.
(48) Ji, D.; Du, Y.; Meng, H.; Zhang, L.; Huang, Z.; Hu, Y.; Li, J.; Yu, F.; Li, Z. A novel colorimetric strategy for sensitive and rapid sensing of ascorbic acid using cobalt oxyhydroxide nanoflakes and 3,3',5,5'-tetramethylbenzidine. *Sens. Actuators, B* **2018**, *256*, 512−519.
(49) Lu, J.; Xiong, Y.; Liao, C.; Ye, F. Colorimetric detection of uric acid in human urine and serum based on peroxidase mimetic activity of MIL-53(Fe). *Anal. Methods* **2015**, *7*, 9894−9899.
(50) Wu, D.; Lu, H.-F.; Xie, H.; Wu, J.; Wang, C.-M.; Zhang, Q.-L. Uricase-stimulated etching of silver nanoprisms for highly selective and sensitive colorimetric detection of uric acid in human serum. *Sens. Actuators, B* **2015**, *221*, 1433−1440.
(51) Fang, A.; Wu, Q.; Lu, Q.; Chen, H.; Li, H.; Liu, M.; Zhang, Y.; Yao, S. Upconversion ratiometric fluorescence and colorimetric dual-readout assay for uric acid. *Biosens. Bioelectron.* **2016**, *86*, 664−670.
(52) Badoei-dalfard, A.; Sohrabi, N.; Karami, Z.; Sargazi, G. Fabrication of an efficient and sensitive colorimetric biosensor based on Uricase/Th-MOF for uric acid sensing in biological samples. *Biosens. Bioelectron.* **2019**, *141*, 111420−111429.
(53) Pal, J.; Pal, T. Enzyme mimicking inorganic hybrid Ni@$MnO_2$ for colorimetric detection of uric acid in serum samples. *RSC Adv.* **2016**, *6*, 83738−83747.
(54) He, Y.; Qi, F.; Niu, X.; Zhang, W.; Zhang, X.; Pan, J. Uricase-free on-demand colorimetric biosensing of uric acid enabled by integrated CoP nanosheet arrays as a monolithic peroxidase mimic. *Anal. Chim. Acta* **2018**, *1021*, 113−120.
(55) Wang, H.; Wan, K.; Shi, X. Recent Advances in Nanozyme Research. *Adv. Mater.* **2018**, *31*, 1805368.


https://dx.doi.org/10.1021/acsbiomaterials.9b01922
*ACS Biomater. Sci. Eng.* 2020, 6, 1438−1448